Journal of Advanced Ceramics
2021, **10**(1): 120–128
https://doi.org/10.1007/s40145-020-0425-2

ISSN 2226-4108
CN 10-1154/TQ

Research Article

Novel optical properties and induced magnetic moments in Ru-doped hybrid improper ferroelectric $Ca_3Ti_2O_7$

Xingxing WU[a], Shouyu WANG[b,*], Winnie WONG-NG[c], Qiang GU[a], Yao JIANG[a], Chao WANG[a], Shuang MA[b], Weifang LIU[a,*]

[a]*Tianjin Key Laboratory of Low Dimensional Materials Physics and Preparing Technology, School of Science, Tianjin University, Tianjin 300072, China*
[b]*College of Physics and Material Science, Tianjin Normal University, Tianjin 300074, China*
[c]*Materials Measurement Science Division, National Institute of Standards and Technology, Gaithersburg, Maryland 20899, USA*

Received: March 7, 2020; Revised: September 5, 2020; Accepted: September 9, 2020

Abstract: Hybrid improper ferroelectric $Ca_3Ti_2O_7$ and $Ca_3Ti_{1.9}Ru_{0.1}O_7$ ceramics were successfully synthesized by conventional solid-state reaction method. Two strongest diffraction peaks located around $2\theta = 33°$ shifted towards the lower angle region with Ru substitution, reflecting structure variation. Grain growth and higher oxygen vacancy concentration after doping resulted in a reduction in the coercive field about 20 kV/cm. Optical bandgap estimated by UV−vis diffuse reflectance (DR) spectrum and X-ray photoelectron spectroscopy (XPS) valence band spectra showed a decreasing trend due to the existence of impurity energy level upon Ru doping, which was consistent with the results of first-principles calculations. The origin of the unexpected induced magnetic moments in Ru-dope $Ca_3Ti_2O_7$ is also discussed.

Keywords: oxides; electronic materials; optical properties; X-ray diffraction; defects; lectronic structure; ferroelectricity

1 Introduction

In recent years, hybrid improper ferroelectricity (HIF) has been investigated extensively due to its promising applications in creating room-temperature multiferroic materials with strong magnetoelectric coupling [1–3]. The term "hybrid" improper ferroelectricity is used to describe the two kinds of octahedron rotations, and the main feature of HIF is the combination of coherent oxygen octahedral rotation ($a^0a^0c^+$ in Glazer's notation) and tilting ($a^-a^-c^0$) [4,5]. Researchers have proposed that HIF widely exits in artificial superlattices such as $SrTiO_3/PbTiO_3$ and Ruddlesden–Propper structure ($A_{n+1}B_nO_{3n+1}$, RP) [1,2,6–9]. Liu *et al.* [5] and Oh *et al.* [10] also demonstrated experimentally that HIF existing in the RP structures at room temperature. RP structure has become the focus for HIF research since the octahedral tilting and rotation exist extensively in these materials.

$Ca_3Ti_2O_7$ is one of the typical RP structures ($n = 2$) with properties including prominent photocatalytic, special luminescence, and significant hybrid improper

* Corresponding authors.
E-mail: S. Wang, shouyu.wang@yahoo.com;
W. Liu, wfliu@tju.edu.cn

ferroelectric properties [8,11–16]. Recently, researchers are working to improve the ferroelectric properties by doping or substitution. Li *et al.* [17] studied the preferential occupation of A-site substitution and proposed isovalent substitution could enhance ferroelectricity. Huang *et al.* [18] successfully reduced the coercive field by doping Na ions at the A-site and found a novel reversible diode effect. So far, most investigators have focused their research on the substitution of A-site, and only a handful of studies were focused on B-site doping. Liu *et al.* [19] proposed theoretically that B-site doped $Ca_3Ti_2O_7$ reduces polarization with decreased tolerance factor, and they also found the first-order phase transition temperatures of $Ca_3Ti_{2-x}Mn_xO_7$ (x = 0, 0.05, 0.1, 0.15) decrease linearly with increasing Mn doping concentration [5]. In 2012, Gong *et al.* [20] experimentally confirmed that Ru^{4+} is a magnetic ion that enhances ferromagnetic properties in $Bi_{0.9}La_{0.1}FeO_3$ ceramics. However, the influence of ferroelectric and optical properties through B-site substitution has not been extensively studied experimentally.

In this work, we chose Ru^{4+} as the B-site dopant and prepared $Ca_3Ti_2O_7$ and $Ca_3Ti_{1.9}Ru_{0.1}O_7$ ceramics by solid-state synthesis technique. The coercive field was effectively reduced with Ru substitution, suggesting $Ca_3Ti_{1.9}Ru_{0.1}O_7$ is more favorable for practical applications. Interestingly, the magnetization hysteresis loop shows obviously hysteresis after Ru doping and the spin-up and spin-down density of state (DOS) became asymmetric, which indicates weak ferromagnetism was induced, thereby making it possible to achieve room temperature multiferroic materials.

2 Experimental

2. 1 Preparation of the samples

Powders $Ca_3Ti_2O_7$ and $Ca_3Ti_{1.9}Ru_{0.1}O_7$ were synthesized by a conventional solid-state reaction method in air. Appropriate amounts of $CaCO_3$ (99.99%), TiO_2 (99.99%), and ruthenium oxide hydrate (ruthenium content of 75%) were chosen as starting materials and were thoroughly grounded with alcohol and agate balls for 10 h. The mixture was preheated at 1000 ℃ for 10 h and reground to obtain the desired powders. Finally, the powders were pressed into cylindrical compacts under uniaxial compression and sintered at 1450 and 1460 ℃ in air for 30 h to obtain the dense $Ca_3Ti_2O_7$ and $Ca_3Ti_{1.9}Ru_{0.1}O_7$ ceramics.

2. 2 Characterizations of the samples

Crystal structure analysis of the samples was carried out by X-ray diffraction (XRD, Rigaku D/MAX-2500 diffractometer with Cu Kα radiation). Microstructures were investigated by scanning electron microscopy (SEM) using a model SU8010 field-emission scanning electron microscope (Hitachi Co., Tokyo, Japan). To analyze the chemical states of the constituents and the content of surface elements, X-ray photoelectron spectroscopy (XPS) was performed using a PHI1600 spectrometer (U1vac-Phi Co., Chigasaki, Kanagawa, Japan). Silver was placed on both sides of ceramics for the electrical property testing, using an Axiacct TF2000 ferroelectric analyzer (aixACCT Co., Aachen, Germany). UV−vis diffuse reflectance (DR) spectrums were recorded with a UV-3600UV-VIS-NIR spectrophotometer (Shimadzu Co., Tokyo, Japan). The magnetization hysteresis (M–H) loops of the samples at room temperature were made with a SQUID-VSM magnetic property measurement system (Quantum Design Co., San Diego, CA, USA). First-principles calculations were performed using Vienna *ab initio* Simulation Package (VASP) with projector augmented wave (PAW) potentials. The exchange–correlation interaction was treated by Perdew–Burke–Ernaerhof (GGA-PBE) with a plane wave energy cut off of 500 eV. To study the change of bandgap, the unit cell with 5×1×5 Monkhorst–Pack k-point mesh was used to calculate density of state (DOS) and differential charge density on $Ca_3Ti_2O_7$ and Ru-doped samples.

3 Results and discussion

3. 1 Crystal structure characterization

The XRD patterns of $Ca_3Ti_2O_7$ and $Ca_3Ti_{1.9}Ru_{0.1}O_7$ after Rietveld refinement process using FULLPROF software are illustrated in Fig. 1(a) [21]. All peaks in the diffraction patterns could be matched perfectly with those of $Ca_3Ti_2O_7$ (space group $A2_1am$ (No. 36)) [22]. Absence of additional peaks indicates Ru atoms replaced Ti atoms successfully. It is obvious that the two strongest peaks located at around $2\theta = 33°$ shifted towards the lower angle region with the Ru doping (Fig. 1(b)), implying changes of the unit cell parameters. Detailed analysis of the structural parameters using the Rietveld refinement is given in Table 1. It can be seen that a, b, and V increased with Ru substitution, which is consistent with the theoretical prediction since the ionic radius of

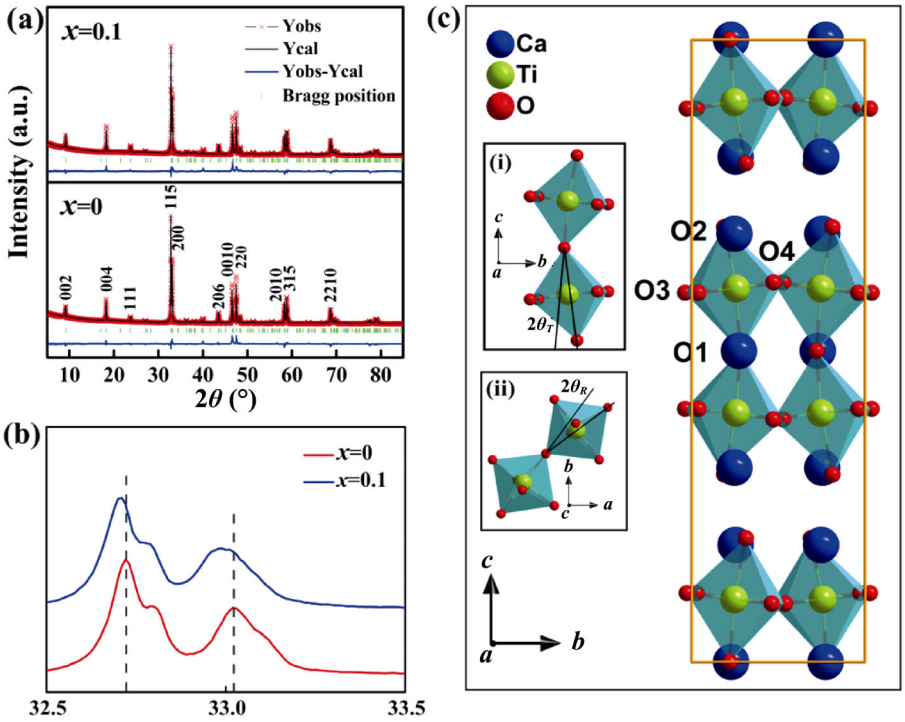

Fig. 1 (a) Rietveld refined XRD patterns of $Ca_3Ti_{2-x}Ru_xO_7$ (x = 0, 0.1) samples. (b) Enlarged views of the diffraction peaks located at about 33°. (c) Crystal structure of $Ca_3Ti_2O_7$. The upper insets are the oxygen octahedral tilt angle θ_T and oxygen octahedral rotation angle θ_R respectively.

Table 1 Structure parameters obtained from Rietveld refinement of $Ca_3Ti_2O_7$ and $Ca_3Ti_{1.9}Ru_{0.1}O_7$

x	a (Å)	b (Å)	c (Å)	V (Å^3)	Ti–O1/Ti–O2	Ti–O3/Ti–O4	Ti–O1–Ti	χ^2
0	5.42302(14)	5.41764(14)	19.51445(41)	573.334	1.9872/1.9588	1.9686/1.9700	159.641	3.55
0.1	5.42913(13)	5.42143(13)	19.50931(39)	574.230	1.9868/1.9584	1.9705/1.9719	159.614	3.20

Ru (radius = 0.620 Å) [23] is slightly larger than that of Ti (radius = 0.605 Å) [24]. However, the lattice shrinking along c direction is likely caused by the decrease of the vertical Ti–O1 (O2) bond lengths and Ti–O1–Ti bond angles. The elongation of the in-plane Ti–O3 (O4) bond length can be attributed to the pressure of vertical plane and expanded volume. The variation of bond lengths and bond angle reflects the distortion of the oxygen octahedra. The crystal structures of $Ca_3Ti_{2-x}Ru_xO_7$ (x = 0, 0.1) ceramics projected on different planes are shown in the insets of Fig. 1(c). For $Ca_3Ti_2O_7$, the oxygen octahedral rotation angle (θ_R) and tilt angle (θ_T) are 9.846° and 10.180°, respectively. While for $Ca_3Ti_{1.9}Ru_{0.1}O_7$, the values of θ_R and θ_T are 9.842° and 10.193°, respectively. According to the formula: $P \propto \alpha Q_R Q_T$ (where P is spontaneous polarization, α represents the coupling coefficient, and Q_R and Q_T are amplitude of rotation and tilt respectively) [25]. The angle of tilt mode increased after Ru doping, so the spontaneous polarization may be improved in $Ca_3Ti_{1.9}Ru_{0.1}O_7$.

3.2 Ferroelectricity research

The most important feature of ferroelectric materials is their ability to reverse their polarization state under the applied electric field, appearing as a hysteresis loop with a corresponding electric field (P–E). P–E loop can be easily affected by temperature, and magnitude and frequency of the applied electric field [26]. Key ferroelectric parameters, such as the remnant polarization P_r and coercive electric field E_c are obtained from these measurements. However, since the polarization of ferroelectrics is not saturated, the uncertainty of the coercive electric field obtained from the P–E loop is somewhat greater. Thus, displacement current verses electrical field (I–E) loops were also shown in the figures. The displacement current involves three parts: leakage current, ferroelectric domain switching, and dielectric displacement. As shown in Figs. 2(a) and

2(b), the current exhibits an obvious peak under Dynamically Hysteresis Method (DHM), which indicates domain switching and confirms its ferroelectric characteristic [27]. Since the positive up negative down (PUND) method can remove the nonhysteretic components, *P*–*E* and *I*–*E* loops of $Ca_3Ti_{2-x}Ru_xO_7$ (x = 0, 0.1) ceramics were obtained by PUND measurement and shown in Figs. 2(c) and 2(d). The coercive field decreased from about 120 to 100 kV/cm after Ru doping. The remnant polarization values of the $Ca_3Ti_2O_7$ and $Ca_3Ti_{1.9}Ru_{0.1}O_7$ samples are 1.6 and 4.4 μC/cm^2 respectively, which indicate the enhancement of polarization via Ru doping. The result is consistent with the above structure analysis.

3. 3 Microstructure characterization

In order to analyze the cause of reduced coercive field in $Ca_3Ti_{1.9}Ru_{0.1}O_7$, the grain size of this material was characterized by SEM. The SEM images and corresponding size distribution histogram of both samples are shown in Fig. 3. It can be seen that both samples show approximate flake-like shape grains and the

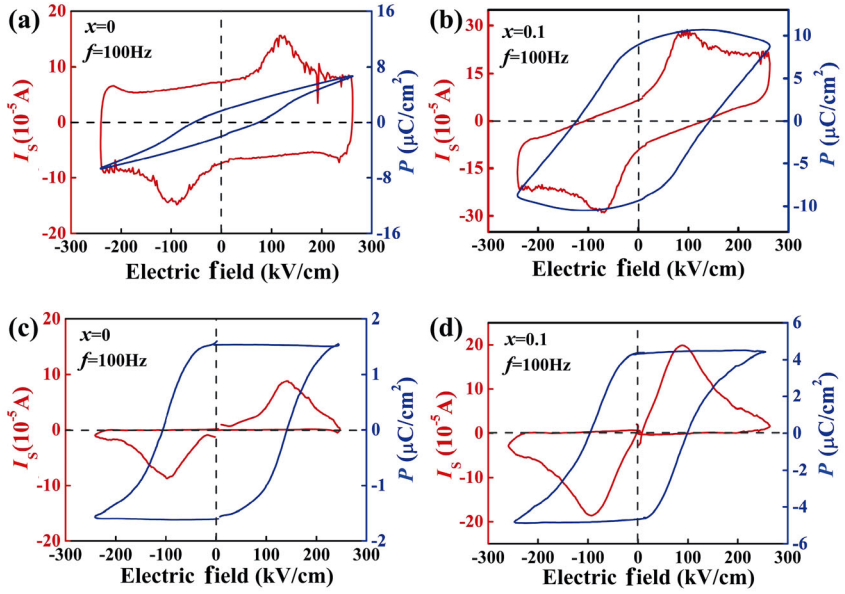

Fig. 2 *P*–*E* loops and displacement current recorded at frequency of 100 Hz in DHM mode for (a) $Ca_3Ti_2O_7$, (b) $Ca_3Ti_{1.9}Ru_{0.1}O_7$. *P*–*E* loops of $Ca_3Ti_2O_7$ and $Ca_3Ti_{1.9}Ru_{0.1}O_7$ ceramics obtained by PUND measurement for (c) and (d), respectively.

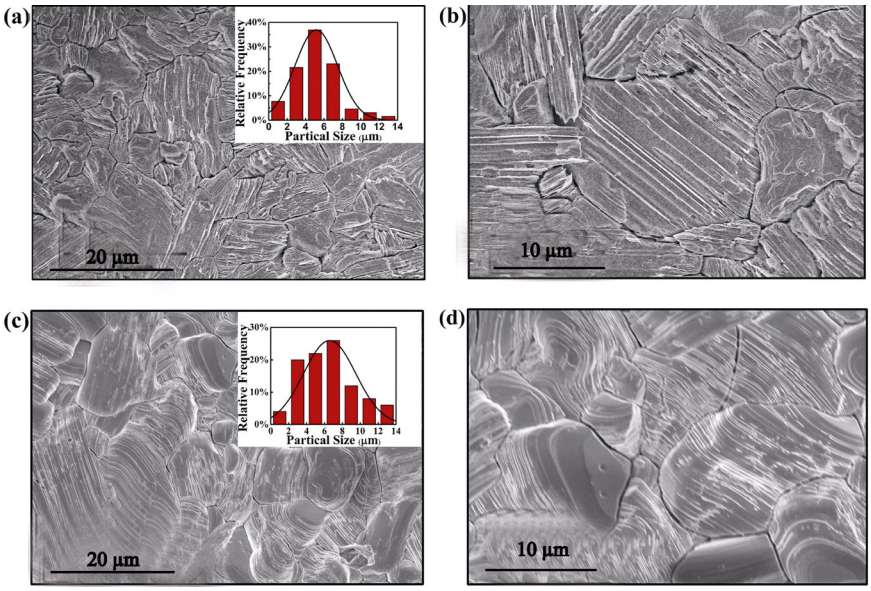

Fig. 3 SEM images of (a, b) $Ca_3Ti_2O_7$ ceramic and (c, d) $Ca_3Ti_{1.9}Ru_{0.1}O_7$ ceramic. The upper insets are the corresponding statistic particle size distribution of $Ca_3Ti_{2-x}Ru_xO_7$ (x = 0, 0.1) samples.

thickness varies from 1 to 14 μm, with the average size increased from 5.33 to 6.85 μm after Ru doping. In ferroelectric ceramics, the crystallite grains are randomly oriented and contain multiple ferroelectric domains. When domains in a grain attempt to switch under an external electric field, they are constrained by adjacent grains of different orientations [27,28]. This causes the E_c values of ceramics with smaller grains much higher than ceramics with large grains. Besides, the lager grain size of $Ca_3Ti_{1.9}Ru_{0.1}O_7$ ceramic can effectively improve the ferroelectric polarization due to fewer grain boundaries in the same area, which resulted in weakened influence of the domain pinning effect [29,30].

3. 4 Valence state and element content analysis

Oxygen vacancy concentration is another factor affecting the coercive field. XPS measurements were carried out and the spectra of Ca 2p, O 1s, and Ti 3d core level fitted by Lorentzian–Gaussian functions are presented in Fig. 4, where the core level binding energies were aligned with respect to C 1s peak (284.6 eV). The O 1s core level regions are fitted to 3 peaks at about 529.3, 531.3, and 532.4 eV in Fig. 4(b). The first line (red) is attributed to the oxygen present in the lattice and the second line (blue) is related to the oxygen deficient regions [31,32]. The last one (green) corresponds to adsorbed molecular water [33]. Since oxygen vacancy plays an important role in modifying physical properties and optical properties, we elucidate the variations of defects by using a semiquantitative formula. The relative concentration of lattice oxygen could be described by the following formula [34]:

$$C_x = \frac{I_x}{S_x} / \sum_i \frac{I_i}{S_i} \tag{1}$$

where C_x is the concentration of the measured atom, I_x is the intensity of the peak corresponding to the measured elements, S_x is the sensitivity factor of the measured elements, and S_i is that of the ith element. The calculated atom ratio of O/Ca in $Ca_3Ti_2O_7$ sample is 2.06, which is smaller than the stoichiometric ratio of 2.33. It is well known that calcination will introduce oxygen vacancies at high temperature. For $Ca_3Ti_{1.9}Ru_{0.1}O_7$ sample, the atom ratio of O/Ca is calculated to be 1.90, indicating more oxygen vacancies are introduced after the Ru doping. The domain cores were more likely to be formed around defective regions. As the electric field is enhanced, the domain walls begin to move in the direction of the electric field, while these walls also expand widthwise [35]. Thus, the domain volume fraction along the direction of the electric field is increased and the opposite domain volume fraction is reduced until it becomes a single domain, which explains the decrease of coercive field by Ru doping. The fitted Ti 2p spectra are shown in Fig. 4(c), where binding energy peaks of Ti 2p3/2 located at about 457.8 and 456.8 eV correspond to the Ti^{4+} and Ti^{3+} respectively [36]. For $Ca_3Ti_2O_7$ and $Ca_3Ti_{1.9}Ru_{0.1}O_7$, the ratio of Ti^{3+}/Ti^{4+} is calculated as 0.18 and 0.26, which demonstrates the concentration of Ti^{3+} increases with Ru doping. Some tetravalent titanium ions are converted to trivalent during the preparation process and the tendency is enhanced further after doping with Ru, which can be described as follow:

$$Ti^{4+} + e' \rightarrow Ti^{3+} \tag{2}$$

The combination of trivalent titanium and lattice oxygen makes more oxygen vacancy be produced. This process can be illustrated by the following steps:

$$2Ti^{3+} + 3O^{2-} \rightarrow 2(Ti_{Ti^{4+}})' + 2h^{\bullet} + 3O_O^{\times} \tag{3}$$

$$2O^{2-} + 4h^{\bullet} \rightarrow O_2 \uparrow + V_O \tag{4}$$

Here, $h^{\bullet}$ denotes hole and V_O represents oxygen vacancy.

The leakage current density versus applied electric field (J–E) is given in Fig. 4(d). One notes that the leakage current is increased significantly after Ru doping, which can be attributed to the influence of oxygen vacancies whose main function is to introduce carriers. The main process can be expressed by

$$V_O \rightarrow V_O^{\bullet} + e' \tag{5}$$

$$V_O^{\bullet} \rightarrow V_O^{\bullet\bullet} + e' \tag{6}$$

Thus, Ru substitution increases the ionized oxygen vacancy ($V_O^{\bullet}$ or $V_O^{\bullet\bullet}$), the conducting electron (e'), and the hole ($h^{\bullet}$). The combination of these species is eventually, responsible for the high leakage current in $Ca_3Ti_{1.9}Ru_{0.1}O_7$.

3. 5 Optical and magnetic property analysis

It is common knowledge that the doping will influence optical properties; therefore, the optical properties of the $Ca_3Ti_{2-x}Ru_xO_7$ (x = 0, 0.1) were obtained by UV–vis DR spectra at room temperature (Fig. 5(a)). The data were collected with reference to a $BaSO_4$ standard. We note that $Ca_3Ti_2O_7$ has strong absorption

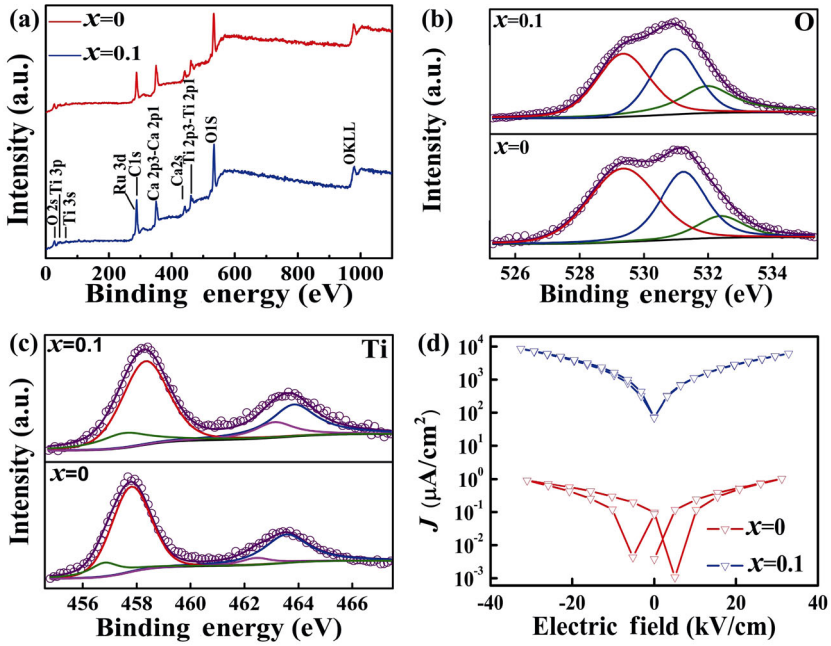

Fig. 4 XPS spectra of (a) full spectrum, (b) O 1s, and (c) Ti 2p for $Ca_3Ti_{2-x}Ru_xO_7$ (x = 0, 0.1) samples. (d) Leakage current data for $Ca_3Ti_2O_7$ and $Ca_3Ti_{1.9}Ru_{0.1}O_7$.

in the range of 300–400 nm; however, there are two absorption edges in the $Ca_3Ti_{1.9}Ru_{0.1}O_7$ sample, and the band gap of $Ca_3Ti_{1.9}Ru_{0.1}O_7$ reduced greatly relative to that of $Ca_3Ti_2O_7$. Figure 5(b) gives the valence band XPS of $Ca_3Ti_{2-x}Ru_xO_7$ (x = 0, 0.1). The valence band maximum was estimated to be around 1.39 eV for $Ca_3Ti_2O_7$, while $Ca_3Ti_{1.9}Ru_{0.1}O_7$ showed notable differences: the main absorption is located at 0.54 eV, whereas an unusual maximum energy associated with the band tail blue-shifts towards the vacuum level at about −1.52 eV. It was reported that in black TiO_2 nanoparticles, the band tail is attributed to the defect band formed by oxygen vacancy [37]. Based on this report, we carried out first-principles calculation to verify the contribution of the band tail in $Ca_3Ti_{1.9}Ru_{0.1}O_7$.

Field-dependent magnetizations were recorded at room temperature to explore the magnetic properties. Figure 6 shows the magnetization hysteresis loops of $Ca_3Ti_{2-x}Ru_xO_7$ (x = 0, 0.1) with an applied field up to a maximum of 25 kOe. The obvious hysteresis after Ru doping demonstrates the existence of a weak ferromagnetic component, which can be attributed to the special valence electron configuration of Ru ions ($4d^4$). In RuO_6 octahedron, the d orbitals of Ru^{4+} can be divided into two high-level e_g orbitals and three low-level t_{2g} orbitals under the influence of ligand field. The electrons in d orbitals of Ru^{4+} are preferable to low-spin state occupation and the electron configuration is $(t_{2g})^4$, which is consistent with the following theoretical calculation (the magnetic moment of Ru is calculated to be about 1.37μ_B). It has been reported that the magnetism is increased with Ru substitution in varied systems [38,39]; therefore Ru doping is of great significance in improving the magnetic properties of materials.

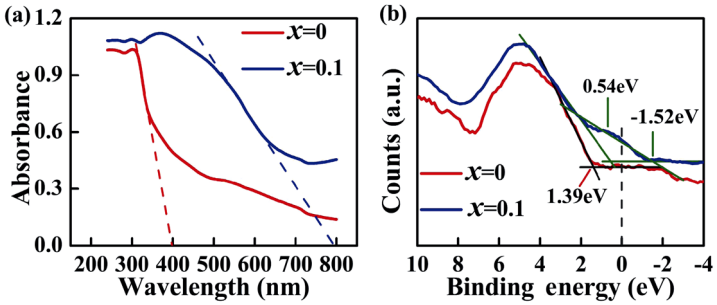

Fig. 5 (a) UV–vis DR spectra of $Ca_3Ti_{2-x}Ru_xO_7$ (x = 0, 0.1) samples. (b) XPS valence band spectra for $Ca_3Ti_2O_7$ and $Ca_3Ti_{1.9}Ru_{0.1}O_7$ samples.

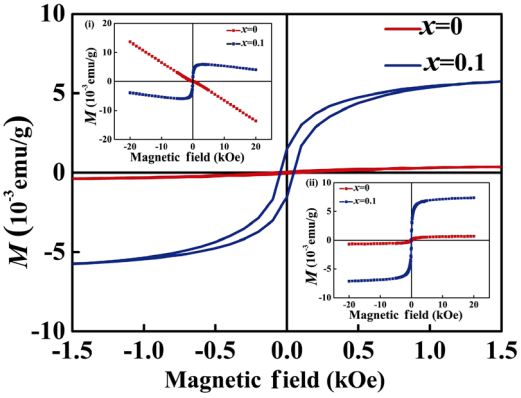

Fig. 6 Field-dependent magnetization hysteresis (*M*–*H*) loops of $Ca_3Ti_{2-x}Ru_xO_7$ (x = 0, 0.1) ceramics in low field at room temperature. Insets: (i) raw data of *M*–*H* loop with an applied field up to a maximum of 25 kOe; (ii) *M*–*H* loops in which diamagnetism were removed.

3. 6 First-principles calculation

3.6.1 DOS analysis

The first-principles calculation was conducted to analyze the DOS and electronic structure. DOS calculations were performed for two compositions: (i) pure $Ca_3Ti_2O_7$ unit cell and (ii) Ru-doped unite cell (a Ti atom was substituted by a Ru atom in a unit cell). The results are shown in Figs. 7(a) and 7(b). The valence band is mainly composed of the O 2p states. The conduction band in the range from 2.5 to 4 eV is mainly contributed by the Ti 3d and O 2p states. Compared with $Ca_3Ti_2O_7$, the impurity energy level appears from –2 to 1 eV in Ru-doped $Ca_3Ti_2O_7$, which is comprised by Ru 3d and O 2p states and distributes on both sides of the Fermi level. The band gap of Ru-doped $Ca_3Ti_2O_7$ is much smaller than that of $Ca_3Ti_2O_7$ (2.35 eV) because of the presence of impurity energy level. As can be seen from the DOS, the band tail in the valence band spectrum is composed of impurity levels.

Interestingly, the spin-up and spin-down DOS become asymmetric in Fig. 7(b), thereby resulting in significant spin splitting, which indicates magnetic moments are induced due to Ru substitution. The total magnetic moments of different atoms are summarized in Table 2. It is obvious that the major contribution comes from Ru atom and partly derives from O and Ru atom hybridization. To understand the origin of the magnetic moments, the DOS of Ru^{4+} in RuO_2 and Ru-doped $Ca_3Ti_2O_7$ are also shown in Figs. 7(c) and 7(d) respectively. Ru^{4+} of RuO_2 is a non-spin polarizer, while in Ru substitution systems, the originally non-polarized Ru^{4+} 4d orbitals produce spin polarization due to orbital hybridization with the surrounding O atoms.

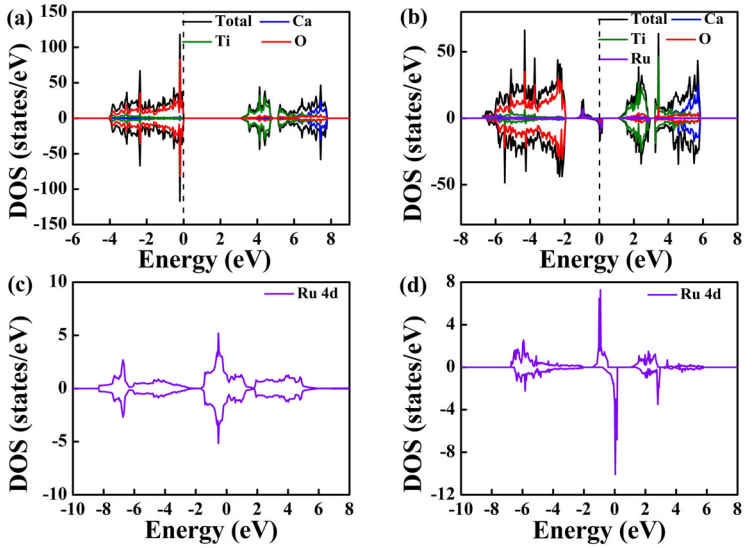

Fig. 7 DOS of (a) pure $Ca_3Ti_2O_7$, (b) Ru-doped $Ca_3Ti_2O_7$; DOS of Ru^{4+} in (c) RuO_2 and (d) Ru-doped $Ca_3Ti_2O_7$.

Table 2 Contributions of magnetic moment from each atom

Atom	Ru	O_I	O_{II}	O_{III}	O_{IV}	O_V	O_{VI}	O_{VII}	Ti	Total
M (μ_B)	1.37	0.02	0.06	0.06	0.11	0.05	0.05	0.09	–0.01	1.80

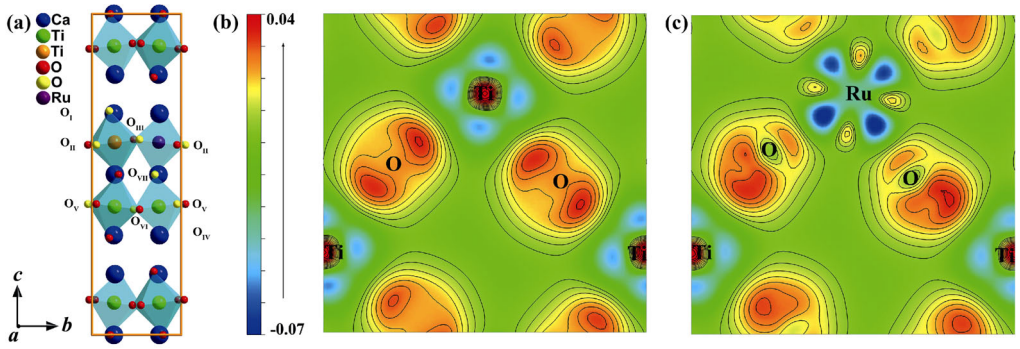

Fig. 8 (a) Model of magnetic moment distribution, where yellow, orange, and violet atoms represent magnetic moment produced by O, Ti, and Ru atoms, respectively. The charge density difference of the stable interface along (010) plane for (b) $Ca_3Ti_2O_7$ and (c) Ru-doped $Ca_3Ti_2O_7$. The red and blue colors represent charge accumulation and depletion respectively.

3.6.2 Differential charge density studies

In order to further explore the bonding properties between Ti and O atoms upon Ru doping, differential charge density of the plane (010) was plotted in Figs. 8(b) and 8(c). Increased charge concentration around oxygen atoms near the titanium atom was found after Ru doping, which reflects that the ionic character is slightly enhanced for the Ti–O bonds and the concentration of oxygen vacancies is higher after Ru doping. These results are consistent with those of XPS.

The materials with Ru doping render the room temperature multiferroic possible and can be applied more readily in low-power-consumption spintronics devices [40].

4 Conclusions

To summarize, $Ca_3Ti_2O_7$ and $Ca_3Ti_{1.9}Ru_{0.1}O_7$ ceramics were successfully prepared by conventional solid-state techniques. The difference of ionic radius between titanium and ruthenium gives rise to the increasing degree of oxygen octahedral tilting and rotation. The decrease of the coercive field was owing to the increase of the oxygen vacancy concentration and grain growth. On the other hand, the introduction of oxygen vacancy increased the leakage current significantly. Optical properties such as size and location of band gaps were obtained by UV–vis measurements and first-principles calculations. Both experimental and theoretical results showed that the band gap is much smaller in $Ca_3Ti_{1.9}Ru_{0.1}O_7$ compared with $Ca_3Ti_2O_7$, which is due to the hybridization of oxygen and ruthenium atoms after doping. At the same time, the B-site substitution of Ru element induces weak ferromagnetism, which is of great significance as it broadens the applications of the RP-perovskites.

Acknowledgements

This work was funded by the National Natural Science Foundation of China (51572193), and the Natural Science Foundation of Tianjin (20JCZDJC00210).

References

[1] Benedek NA, Fennie CJ. Hybrid improper ferroelectricity: A mechanism for controllable polarization-magnetization coupling. *Phys Rev Lett* 2011, **106**: 107204.
[2] Bousquet E, Dawber M, Stucki N, *et al*. Improper ferroelectricity in perovskite oxide artificial superlattices. *Nature* 2008, **452**: 732–736.
[3] Oh YS, Luo X, Huang FT, *et al*. Experimental demonstration of hybrid improper ferroelectricity and the presence of abundant charged walls in $(Ca,Sr)_3Ti_2O_7$ crystals. *Nat Mater* 2015, **14**: 407–413.
[4] Glazer AM. The classification of tilted octahedra in perovskites. *Acta Crystallogr B* 1972, **28**: 3384–3392.
[5] Liu XQ, Wu JW, Shi XX, *et al*. Hybrid improper ferroelectricity in Ruddlesden-Popper $Ca_3(Ti,Mn)_2O_7$ ceramics. *Appl Phys Lett* 2015, **106**: 202903.
[6] Ruddlesden SN, Popper P. The compound $Sr_3Ti_2O_7$ and its structure. *Acta Cryst* 1958, **11**: 54–55.
[7] Mulder AT, Benedek NA, Rondinelli JM, *et al*. Turning ABO_3 antiferroelectrics into ferroelectrics: Design rules for practical rotation-driven ferroelectricity in double perovskites and $A_3B_2O_7$ Ruddlesden-Popper compounds. *Adv Funct Mater* 2013, **23**: 4810–4820.
[8] Rondinelli JM, Fennie CJ. Octahedral rotation-induced ferroelectricity in cation ordered perovskites. *Adv Mater* 2012, **24**: 1961–1968.
[9] Zhao HJ, Íñiguez J, Ren W, *et al*. Atomistic theory of hybrid improper ferroelectricity in perovskites. *Phys Rev B* 2014, **89**: 174101.
[10] Oh YS, Luo X, Huang FT, *et al*. Experimental dem-

onstration of hybrid improper ferroelectricity and the presence of abundant charged walls in $(Ca,Sr)_3Ti_2O_7$ crystals. *Nat Mater* 2015, **14**: 407–413.
[11] Nowadnick EA, Fennie CJ. Domains and ferroelectric switching pathways in $Ca_3Ti_2O_7$ from first principles. *Phys Rev B* 2016, **94**: 104105.
[12] Senn MS, Bombardi A, Murray CA, *et al*. Negative thermal expansion in hybrid improper ferroelectric Ruddlesden-Popper perovskites by symmetry trapping. *Phys Rev Lett* 2015, **114**: 035701.
[13] Cherian JG, Birol T, Harms NC, *et al*. Optical spectroscopy and band gap analysis of hybrid improper ferroelectric $Ca_3Ti_2O_7$. *Appl Phys Lett* 2016, **108**: 262901.
[14] Li X, Yang L, Li CF, *et al*. Ultra-low coercive field of improper ferroelectric $Ca_3Ti_2O_7$ epitaxial thin films. *Appl Phys Lett* 2017, **110**: 042901.
[15] Okazaki Y, Mishima T, Nishimoto S, *et al*. Photocatalytic activity of $Ca_3Ti_2O_7$ layered-perovskite doped with Rh under visible light irradiation. *Mater Lett* 2008, **62**: 3337–3340.
[16] Cao RP, Chen G, Yu XG, *et al.* Luminescence properties of $Ca_3Ti_2O_7$:Eu^{3+} , Bi^{3+} , R^+ (R^+ = Li^+, Na^+, and K^+) red emission phosphor. *J Solid State Chem* 2014, **220**: 97–101.
[17] Li CF, Zheng SH, Wang HW, *et al*. Structural transitions in hybrid improper ferroelectric $Ca_3Ti_2O_7$ tuned by site-selective isovalent substitutions: A first-principles study. *Phys Rev B* 2018, **97**: 184105.
[18] Huang C, Wong-Ng W, Liu WF, *et al*. Major improvement of ferroelectric and optical properties in Na-doped Ruddlesden-Popper layered hybrid improper ferroelectric compound, $Ca_3Ti_2O_7$. *J Alloys Compd* 2019, **770**: 582–588.
[19] Liu XQ, Chen BH, Lu JJ, *et al*. Hybrid improper ferroelectricity in B-site substituted $Ca_3Ti_2O_7$: The role of tolerance factor. *Appl Phys Lett* 2018, **113**: 242904.
[20] Gong YF, Wu P, Hai X, *et al.* Enhanced dielectric and magnetic properties in Ru-substituted $Bi_{0.9}La_{0.1}FeO_3$ ceramics. *J Phys D: Appl Phys* 2012, **45**: 355001.
[21] Xu XL, Liu WF, Zhang H, *et al*. The abnormal electrical and optical properties in Na and Ni codoped $BiFeO_3$ nanoparticles. *J Appl Phys* 2015, **117**: 174106.
[22] Li GJ, Liu XQ, Lu JJ, *et al*. Crystal structural evolution and hybrid improper ferroelectricity in Ruddlesden-Popper $Ca_{3-x}Sr_xTi_2O_7$ ceramics. *J Appl Phys* 2018, **123**: 014101.
[23] Yan F, Lai M-O, Lu L, *et al*. Enhanced multiferroic properties and valence effect of Ru-doped $BiFeO_3$ thin films. *J Phys Chem C* 2010, **114**: 6994–6998.
[24] Yu K, Jin L, Li Y, *et al*. Structure and conductivity of perovskite $Li_{0.355}La_{0.35}Sr_{0.3}Ti_{0.995}M0.005O_3$ (M = Al, Co and In) ceramics. *Ceram Int* 2019, **45**: 23941–23947.
[25] Hu ZZ, Lu JJ, Chen BH, *et al*. First-order phase transition and unexpected rigid rotation mode in hybrid improper ferroelectric (La, Al) co-substituted $Ca_3Ti_2O_7$ ceramics. *J Materiomics* 2019, **5**: 618–625.
[26] Jin L, Li F, Zhang SJ. Decoding the fingerprint of ferroelectric loops: Comprehension of the material properties and structures. *J Am Ceram Soc* 2014, **97**: 1–27.
[27] Yan HX, Inam F, Viola G, *et al*. The contribution of electrical conductivity, dielectric permittivity and domain switching in ferroelectric hysteresis loops. *J Adv Dielect* 2011, **1**: 107–118.
[28] Li JY, Rogan RC, Üstündag E, *et al*. Domain switching in polycrystalline ferroelectric ceramics. *Nat Mater* 2005, **4**: 776–781.
[29] Zhang BH, Hu ZZ, Chen BH, *et al*. Improved hybrid improper ferroelectricity in B-site substituted $Ca_3Ti_2O_7$ ceramics with a Ruddlesden–Popper structure. *J Appl Phys* 2020, **128**: 054102.
[30] Zhang QW, Cai W, Li QT, *et al*. Enhanced piezoelectric response of (Ba,Ca)(Ti, Zr)O_3 ceramics by super large grain size and construction of phase boundary. *J Alloys Compd* 2019, **794**: 542–552.
[31] Han YL, Liu WF, Wu P, *et al*. Effect of aliovalent Pd substitution on multiferroic properties in $BiFeO_3$ nanoparticles. *J Alloys Compd* 2016, **661**: 115–121.
[32] Zhang XN, Liu WF, Han YL, *et al*. Novel optical and magnetic properties of Li-doped quasi-2D manganate $Ca_3Mn_2O_7$ particles. *J Mater Chem C* 2017, **5**: 7011–7019.
[33] Dupin J-C, Gonbeau D, Vinatier P, *et al*. Systematic XPS studies of metal oxides, hydroxides and peroxides. *Phys Chem Chem Phys* 2000, **2**: 1319–1324.
[34] Mukhopadhyay SM, Chen TS. Interaction of $PbZr_xTi_{1-x}O_3$ (PZT) with Ni: Role of surface defects. *J Phys D: Appl Phys* 1995, **28**: 2170–2175.
[35] Miller RC, Weinreich G. Mechanism for the sidewise motion of 180° domain walls in barium titanate. *Phys Rev* 1960, **117**: 1460–1466.
[36] Noto LL, Pitale SS, Terblans JJ, *et al*. Surface chemical changes of $CaTiO_3$:Pr^{3+} upon electron beam irradiation. *Phys B: Condens Matter* 2012, **407**: 1517–1520.
[37] Naldoni A, Allieta M, Santangelo S, *et al.* Effect of nature and location of defects on bandgap narrowing in black TiO_2 nanoparticles. *J Am Chem Soc* 2012, **134**: 7600–7603.
[38] Han YL, Liu WF, Xu XL, *et al.* The abnormal optical property and room-temperature exchange bias behavior in Na- and Ru-codoped $BiFeO_3$ nanoparticles. *J Am Ceram Soc* 2016, **99**: 3616–3622.
[39] Lu CL, Chen X, Dong S, *et al*. Ru-doping-induced ferromagnetism in charge-ordered $La_{0.4}Ca_{0.6}MnO_3$. *Phys Rev B* 2009, **79**: 245105.
[40] Tokunaga Y, Furukawa N, Sakai H, *et al*. Composite domain walls in a multiferroic perovskite ferrite. *Nat Mater* 2009, **8**: 558–562.